Study on the steering capability of a meander-line coil EMAT

S Hurrell, P Charlton, S Mosey, O Rees-Lloyd and R Lewis

Electromagnetic acoustic transducers (EMATs) are well-established as a means of ultrasonic wave generation and reception without the use of a mechanical coupling. When comprising a bias magnetic field and a meander-line coil (MLC), these waves propagate at an angle normal to the emission surface. With the appropriate frequency, the propagation pathway of these ultrasonic waves can be steered to a particular angle. This paper presents the methodology used to find the steering limit of an MLC EMAT and the results from simulations and experimental validations on aluminium. The results show that the maximum shear wave amplitude occurred at around 30°, the steering limit was approximately 50° and the simulations were validated by the experimental set-up to a satisfactory degree.

1. Introduction

A key method of non-destructive testing is ultrasonic testing, whereby high-frequency mechanical waves propagate through a material, reflecting off any boundaries they encounter, such as the surface or any defects within the material. One method is through the use of electromagnetic acoustic transducers (EMATs) that can induce ultrasonic waves in electrically conductive and ferromagnetic materials.

An EMAT combines a bias magnetic field, typically from a permanent magnet or electromagnet, with an alternating eddy current field, from a coil of wire carrying an alternating current (AC), to induce forces directly into the material via three transduction methods: Lorentz forces, magnetisation forces and magnetostriction[1,2]. EMATs possess many advantages over ultrasonic testing due to these principles of wave induction, including no requirement for contact with the specimen, no requirement for a facilitative couplant and the ability to operate at high speeds[3,4]. A main disadvantage, however, is their low signal-to-noise ratio (SNR), which has necessitated much research into optimising their design[5-6].

For the purpose of this study, the material used was aluminium, which only induces waves via the Lorentz force transduction due to being non-magnetic. The Lorentz force consists of static and dynamic components due to the magnet's static magnetic flux and the coil's dynamic eddy current density, given as:

$$\vec{F_L} = \vec{J_e} \times \vec{B} \quad .... \text{(1)}$$

where F_L is the Lorentz force density, J_e is the eddy current density and B is the magnetic flux density. The AC of the coils induce eddy currents in the surface of the material and, in the presence of a static magnetic flux, produce periodic alternating forces at the surface of the specimen, generating bulk waves into the material (consisting of shear and compression wave modes)[7-9].

The configuration of the coil and magnet determines the nature of wave that is excited[7]. A common design for angled bulk wave generation is the meander-line coil (MLC) EMAT, consisting of a bias magnetic field normal to the material's surface and an MLC with straight alternating runs between the magnet and material surface.

The angle at which the MLC EMAT excites waves through a material is given as:

$$\theta = \sin^{-1}\left(\frac{v}{2df}\right)................................... \text{(2)}$$

where θ is the angle normal to the surface, v is the speed of the wave, d is the spacing distance between each alternating straight run of the coil and f is the frequency of the AC and the wave. A popular EMAT design that produces angle-beam waves is the periodic permanent magnet (PPM) that generates shear horizontal waves and is well suited in austenitic and coarse-grain material[10]. PPM EMATs have been studied for their beam-steering capabilities via frequency and have been shown to produce maximum amplitudes across a frequency range for a given spacing between magnets[11] and be capable of creating 2D maps of defects present within a given sample[11-14]. Although MLC EMATs generate shear vertical waves, these two technologies share the same theory of angle-beam emission and thus would share similar conclusions.

An increasingly popular method for angle-beam EMATs is phased array (PA), wherein the EMAT coil's variable spacings focus the bulk waves to a specific location within the material[15,16]. Literature exists on the application of MLC EMATs[17-18,10]; however, much of this examines the differences between traditional MLC and PA MLC designs[17-19]. Work carried out regarding the beam-steering MLC EMATs is less common than research into PPM and PA; however, it does support the theory that the ultrasonic bulk waves can be steered by frequency[20].

The focus of this study is to simulate and experimentally validate the shear wave steering capability of an MLC EMAT on aluminium for different steering angles.

2. Model configuration

The simulation model of a 2D MLC EMAT was created using COMSOL 6.0 Multiphysics. The AC/DC and Structural Mechanics software packages had the predefined mathematical capabilities to

enable such a design to take place. Figure 1 shows the 2D simulation geometry of the EMAT consisting of a 20 mm × 20 mm NdFeB-42 permanent magnet and a copper MLC over a 340 mm × 100 mm aluminium block. The transmit-EMAT was positioned 50 mm from the edge of the aluminium block, with an MLC lift-off distance of 0.5 mm and a magnet lift-off distance of 1.0 mm.
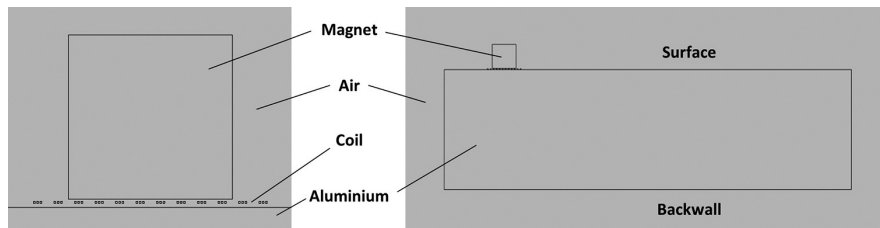

Figure 1. COMSOL simulation model geometry

The speed of the shear and compression waves within the aluminium are 3.12 mm/µs and 6.20 mm/µs, respectively, and according to Snell's Law the angle of the compression wave could be determined for internal mode conversion.

The coil spacing d was set at 2.5 mm, thus according to Equation (2), the angle of the shear wave was entirely controlled by the frequency of the AC. Figure 2 shows the top view of the MLC, with 'Detail A' highlighting that each of the coil's straight runs consists of three thinner strands (0.20 mm × 0.25 mm) with a separation of 0.4 mm. This configuration was chosen as coils made of multiple strands induce a wider eddy current density and, with a square cross-sectional area, also possess a higher conversion efficiency[21]. Figure 2 also shows a 3D model of the MLC as a closed loop (a necessity for COMSOL), but the printed MLC used for the experimental validation had two strands breaking off to be externally powered (shown in Figure 4(a)).
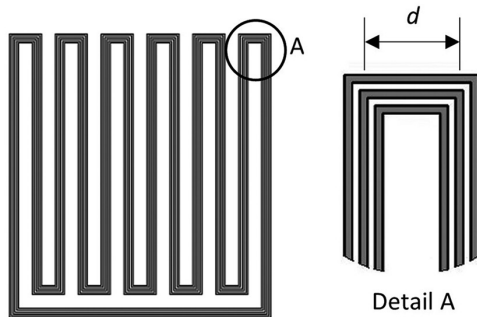

Figure 2. COMSOL simulation 3D MLC geometry

While the simulation was a 2D model, the depth of the coil was specified as the length of the physical coil at 20 mm. The tone-burst current pulse applied to the MLC is given in Equation (3) (adapted from[22]) and was modelled on a Gaussian-sinc pulse:

$$i(t) = Ie^{-\frac{(t-\tau)^2}{2\sigma^2}}\cos\left(2\pi f(t-\tau)\right) \dots\dots\dots (3)$$

where I is the constant current of 6 A, σ is the standard deviation of the pulse, τ is the time delay of the signal's maximum peak and f is the central frequency of the wave. The pulse was designed for any given frequency to start near 0 A and give seven positive peaks before returning to 0 A. This was achieved by making both the

standard deviation and the time delay functions of frequency: $\sigma = 1.2/f$ and $\tau = 5/f$, respectively. The resultant pulse profile for steering angles of 30º and 60º can be seen in Figure 3.

To account for the changing time delay, the arrival time of a wave was taken as the time of the largest peak within a recorded waveform. This also eliminated the need for a predetermined threshold, as a maximum peak would always be present in any waveform. The simulation was set to run from 0-150 µs to account for reflections and any wave mode conversions that would take place within the aluminium specimen. When solving transient models, the relationship between the time-step size and the mesh size must be approximately equal to a Courant number of less than 0.2, given by the Courant-Friedrichs-Lewy (CFL) condition[23], defined as:

$$CFL = \frac{v\Delta t}{h_{max}} \dots\dots\dots\dots\dots\dots\dots\dots (4)$$

where CFL is the Courant number, Δt is the time-step size and h_{max} is the maximum mesh size for the specimen. For 2D COMSOL models, it is recommended to set the maximum mesh size to less than one fifth of the wavelength of the wave (defined as $\lambda = v/f$). For a given steering angle, therefore, the frequency of the wave could be used to calculate the values of maximum mesh size and time-step size, as seen in Table 1.

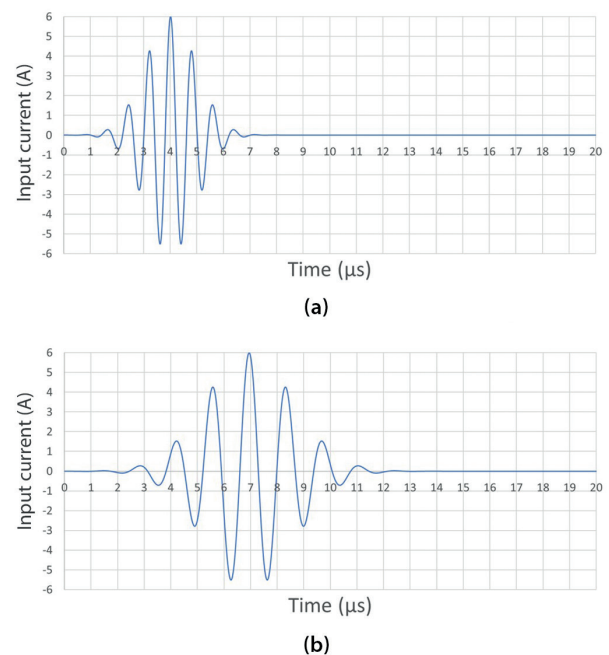Simulation results show bulk waves propagating through the

(a)

(b)

Figure 3. Coil current pulse profiles: (a) coil excitation current: 30° steering angle; and (b) coil excitation current: 60° steering angle

Table 1. Pulse and model variables for a given steering angle

Angle (°)	f (MHz)	σ (× 10⁻⁶)	τ (µs)	h (mm)	Δt (µs)	CFL	L (µH)	C (nF)
15	2.4110	0.50	2.07	0.258	0.010	0.121	1.5160	3.0
30	1.2480	0.96	4.01	0.500	0.020	0.125	1.6621	9.8
45	0.8825	1.36	5.67	0.707	0.024	0.106	1.8534	17.6
60	0.7205	1.67	6.94	0.866	0.030	0.108	2.0600	24.4

(a)
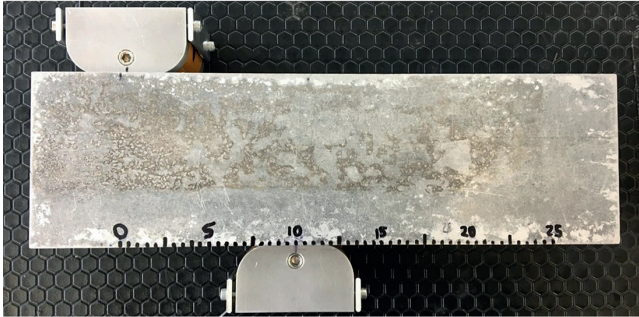
(b)

Figure 4. Experimental MLC design (a) and model set-up design (b)

specimen. The x and y components of displacement were recorded across the specimen's backwall, from x = 0-250 mm at every 5 mm interval (where x = 0 mm and is 50 mm from the edge of the specimen, opposite the transmit-EMAT, as shown in Figure 4(b)). From these values, the x-position of the shear wave's maximum displacement magnitude for each steering angle could be located, thus evaluating the EMAT's steering capability.

3. Experimental validation

An aluminium block, measuring 340 mm × 100 mm × 70 mm, was used with two EMATs (of a similar coil design as in the simulations) in a pitch-catch configuration, as shown in Figure 4(a). The receive-EMAT was in parallel with a decade box, allowing the capacitance to be changed to electrically match the impedance of the RLC circuit for a given steering angle. The values of inductance on the specimen were measured using an impedance analyser and capacitance from Equation (5):

$$C = \frac{1}{(2\pi f)^2 L} \quad\text{.......................................}\ (5)$$

where C is the capacitance, L is the inductance and f is the frequency of the pulse equal to the resonant frequency of the circuit for maximum reception of the receive-EMAT, also in Table 1.

The transmit-EMAT was not in parallel with a decade box, as in real-world applications a standard capacitor would be used that would retain its value. The transmit-EMAT was connected to a pulser system that could emit high-current pulses at the frequencies required. The receive-EMAT was in parallel with an amplifier (of 70 dB gain) due to its low SNR and then to an oscilloscope that would register the signals received by the EMAT.

At the same respective positioning as the simulations, the transmit-EMAT was fixed compressed into a fixed lift-off distance of 1 mm by non-magnetic shims, 50 mm from the edge of the specimen's surface, and the receive-EMAT was placed at the specimen's backwall, from x = 0-250 mm at every 5 mm interval. At each backwall x-position, the receive-EMAT recorded an average 'signal amplitude *versus* time' reading from the oscilloscope, from which the x-position of the shear wave's maximum displacement for each steering angle could be plotted and compared against the simulation values.

4. Results and discussion

Upon the simulation's 2D aluminium block, a colour plot of the von Mises stress was produced at every 0.12 µs time step to create animations of the bulk wave propagations across the entire model's runtime. The stress was plotted instead of displacement due to the better visual quality and Figure 5 shows these plots at their 30 µs time step for each steering angle.

There is little difference in the angle between the simulations for 45° and 60° as it is likely to be nearing the EMAT's steering limit and thus will not increase any further. It is also noticeable that as the steering angle increases, Rayleigh waves start to emerge at the surface for 45° and become the dominant wave at 60°. The different propagation distances of the shear waves from the transmit-EMAT demonstrate the effect of the pulse's time delay on the resulting wave transmission.
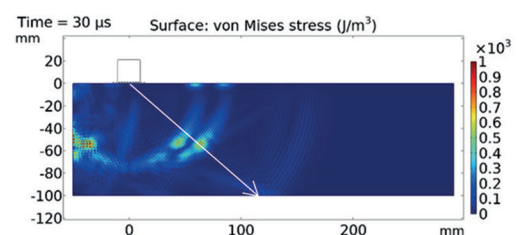
The simulations continued to their end points and the x and y components of displacement were recorded along the specimen's backwall to calculate the displacement magnitude. To better show the shear wave's point of impact, the displacement magnitude values (within an appropriate timeframe of the shear wave's incident on the
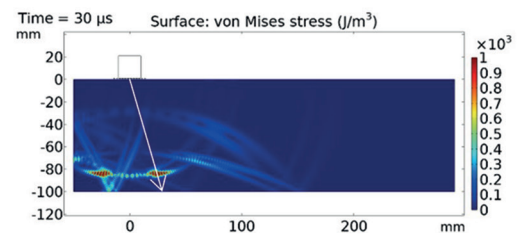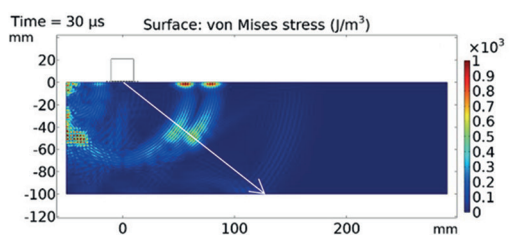

(a)
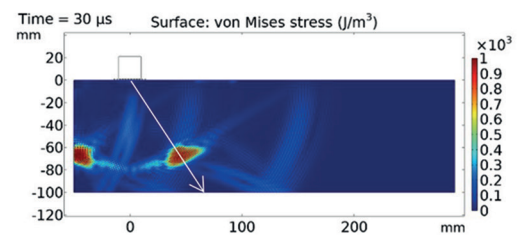
(b)

(c)

(d)

Figure 5. Plots of stress at 30 µs for steering angles of: (a) 15°; (b) 30°; (c) 45°; and (d) 60°

backwall) were processed for the maximum reading at each point. These readings were graphed against their backwall x-position for each steering angle and are shown in Figure 6.

It can be seen from Figure 6 that as the steering angle increases, the x-position of the shear wave's maximum impact also increases. The 15° wave impacts at 30 mm, the 30° wave at 70 mm, the 45° wave at 100 mm and the 60° wave at 115 mm. For the 45° and 60° steering angles, a large peak can be seen near the 0 mm x-position due to the shear waves reflecting from the specimen's sidewall. It can also be seen that the 30° shear wave's maximum displacement is far greater than that of the other steering angles.

Having found the points of maximum shear wave amplitude for all four steering angles, the values of displacement magnitude were graphed against time as A-scans, as shown in Figure 7.

By comparing these A-scans with the colour plots for each steering angle, the peaks of displacement can be identified as waves. The first peak is the initial compression wave directly
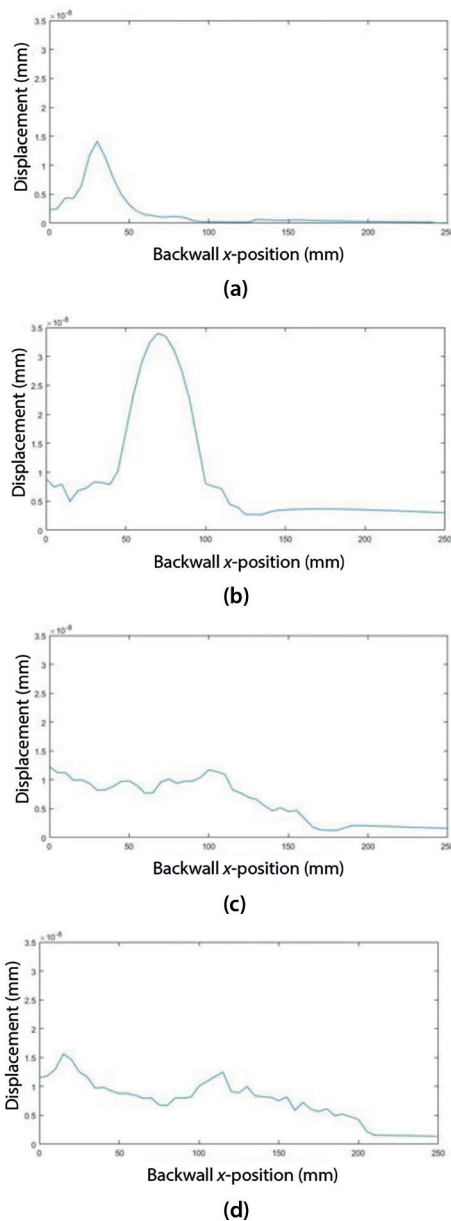
from the transmit-EMAT (peak 1), immediately followed by the compression wave reflected from the sidewall (peak 2). The third and largest peak is the shear wave directly from the transmit-EMAT (peak 3), but for steering angles of 45° and 60° it is clearly seen that these shear wave peaks are composed of two separate peaks (peaks 3a and 3b), as with the initial compression wave peaks for steering angles of 15° and 30° (peaks 1a and 1b). The reason for these two separate peaks is due to the EMAT transmitting two separate shear and Rayleigh waves in each direction, as shown in Figure 5(c)-5(d). These separate waves cannot be distinguished for the 30° steering angle due to their superposition, explaining its far larger shear wave.

Immediately following the direct shear wave peak is a smaller peak that started as a compression wave that struck the sidewall
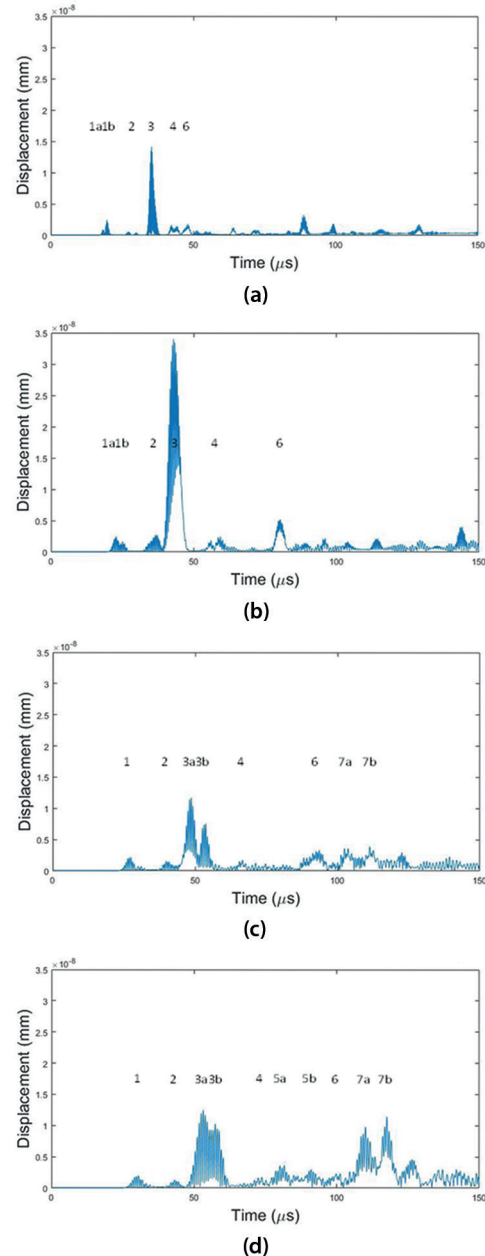

Figure 6. Graphs of maximum displacement magnitude *versus* backwall *x*-position for each steering angle: (a) 15° steering angle; (b) 30° steering angle; (c) 45° steering angle; and (d) 60° steering angle

Figure 7. Graphs of displacement magnitude *versus* time at the *x*-position of maximum impact for each steering angle: (a) 15° steering angle: displacement at *x* = 30 mm; (b) 30° steering angle: displacement at *x* = 70 mm; 30° steering angle: displacement at *x* = 70 mm; (c) 45° steering angle: displacement at *x* = 100 mm; and (d) 60° steering angle: displacement at *x* = 115 mm

and converted into a shear wave (peak 4). For the 60º steering angle, there are two peaks following the refracted shear peaks, found to be the shear waves reflected off the sidewall and, likewise with the direct shear waves, these have two separate components (peaks 5a and 5b). For all the simulations there is a peak that was found to be a small Rayleigh wave (peak 6). Unlike conventional MLC EMAT Rayleigh wave transmission that has a steering angle of 90º, these Rayleigh waves were generated by the shear waves (compression waves for 15º, explaining its earlier arrival time) striking the bottom-left corner of the specimen. Following these induced Rayleigh waves for the 45º and 60º steering angles are the Rayleigh waves that were transmitted due to their higher angles, that also possess separate components (peaks 7a and 7b).

An important factor with the 15º steering angle is the presence of internal mode conversions. Due to the low shear wave angle, the EMAT would also transmit a compression wave at an angle of approximately 31º (according to Snell's Law), which was shallow enough to be seen within the specimen. While the x-position of the shear wave's maximum displacement magnitude was located at 30 mm, the x-position of the compression wave's maximum displacement was located at 50 mm. By looking at the x and y components of displacement at these backwall x-positions, the nature of these two waves can be better seen, as shown in Figure 8.

At 30 mm and 35.31 μs (the time of the shear wave's largest displacement magnitude), the recorded x and y components of displacement were 1.2908×10^{-8} mm and 3.4897×10^{-9} mm, respectively. The particle motion of shear waves is perpendicular to the direction of propagation, which is supported by Figure 8, where the x-component is almost four times larger than the y-component at the time of impact. The same principle can be applied to the compression wave at 50 mm and 20.69 μs with a parallel particle motion, supported by Figure 8 where the x-component is approximately half that of the y-component. Given that the angles of the compression and shear waves are both shallow enough to cause internal mode conversion, by recording the maximum values of stress at each 0.1 mm × 0.1 mm area interval across the 150 μs runtime, their internal wave propagation pathways between surfaces could be plotted, as shown in Figure 9.

As shown in Figure 9, the largest wave path is the shear wave that travels directly from the transmit-EMAT to the backwall 100 mm
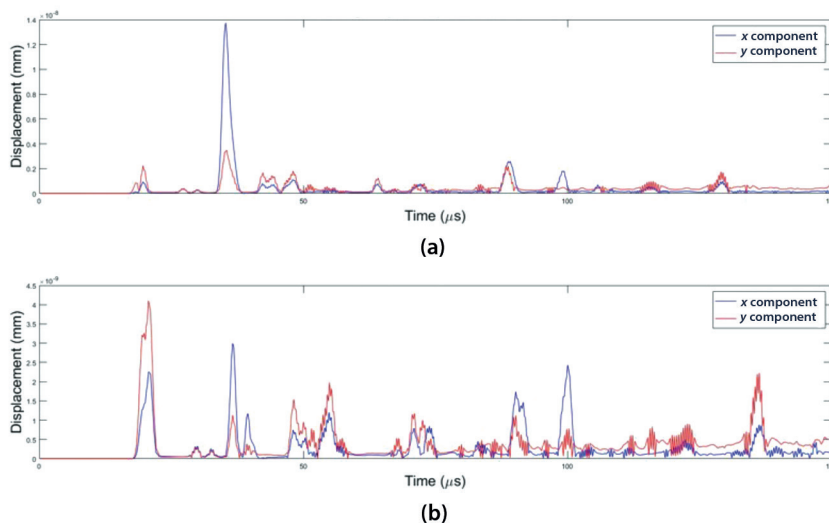
down and 30 mm across. The displacement magnitude on the backwall at this point was 1.4145×10^{-8} mm at 35.31 μs. The second largest wave to hit the backwall came from the combination of two shear waves and one compression wave that reflected from the backwall and then the surface, while mode converting once. The combined result of the shear-shear-compression, shear-compression-shear and compression-shear-shear waves on the backwall was a displacement magnitude of 5.3977×10^{-9} mm, almost half of the displacement magnitude from the direct shear pathway, at 110 mm and 87.16 μs. The different wave combinations that hit the backwall can be seen in Figure 9 and Table 2.
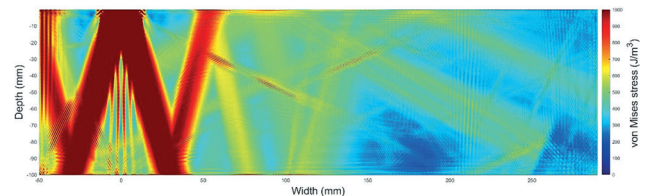

Figure 9. Plot of maximum stress across time for a 15º steering angle

There were some variations when replicating these simulations in experimental validations. Firstly, the Gaussian and sinc pulse used for the models was unable to be implemented with the pulser system. Instead, a rectangular envelope of the same frequency for a given angle, containing approximately 20 peaks, was emitted starting at $t = 0$ μs. This would transmit stronger waves due to containing more peaks at a higher current, which would compensate for the realistic conditions of the practical test and produce an improved SNR.

Additionally, rather than arbitrary probes taking readings every 5 mm across the backwall, a receive-EMAT identical to the transmit-EMAT may produce some inconsistency within the results as the exact lift-off distance may vary.

Finally, the presence of electrical noise within the laboratory equipment would likely mask the signal amplitude of the received wave. Using an oscilloscope, any received wave should have a larger amplitude and a different frequency to the baseline signal noise after the pulse. It is necessary then to put the received signal through a filter to attenuate as much noise as possible. Figure 10 shows an example of the oscilloscope's recorded signal for a 45º steering angle. This signal includes its emission pulse followed by the irregularities of received ultrasound at that x-position. Figure 10 also shows the discrete Fourier transform (DFT) of the signal after 20 μs, as no shear waves could hit the backwall before this time and thus no useful data would be present.

The largest peak within the DFT is approximately the pulse's frequency, followed by smaller peaks at integer scale factors of this frequency. The frequency peaks nearing 0 MHz were likely to be due to electrical noise and could be filtered out. A band-pass filter with a frequency range of the emission pulse's frequency ±0.1 MHz (for a 45º steering angle, the band-pass filter was set to 0.7825-0.9825 MHz) was used to remove the noise. Once filtered, a wave could be seen at approximately 50 μs, which, for a wave at 45º and a distance of 100 mm deep and 100 mm across with a shear wave speed of 3.12 mm/μs, supports

(a)

(b)

Figure 8. Graphs of x and y component displacements for the 15º steering angle, at x-positions of: (a) 30 mm; and (b) 50 mm

Table 2. Largest wave combinations for a 15º steering angle

Wave combinations	Backwall x-position (mm)	Time of arrival (µs)	Displacement magnitude (mm)	Normalised amplitude
S	30	35.31	1.4145×10^{-8}	100.0
P	50	20.69	4.1751×10^{-9}	29.5
SSS	80	101.40	5.1746×10^{-9}	36.6
PSS, SPS, SSP	110	87.16	5.3977×10^{-9}	38.2
PPS, PSP, SPP	140	72.41	2.5387×10^{-9}	17.9
PPP	145	56.85	1.5995×10^{-9}	11.3

that this is the direct shear wave. Figure 11 shows the original and filtered signal after 20 µs.

This process of signal filtering was repeated for all four steering angle experiments at each of their backwall x-positions. The resultant filtered signals' absolute values could produce an upper envelope from the peaks, which could then be compared to the displacement graphs of Figure 7. These envelope graphs at the x-position of maximum simulated displacement for the four steering angles, as stated in Figure 6, can be seen in Figure 12.

When comparing Figure 12 to Figure 7, there are very obvious similarities present. The largest peaks present in both Figures occur at similar times, respective for a given steering angle. There is a slight delay at the time these peaks occur, likely to be due to the different pulses that emit them. There is an irregularity to the size of these

(a)

(b)

Figure 10. Graphs of raw signal amplitude *versus* time and DFT for a 45º steering angle: (a) complete signal at x = 100 mm; and (b) discrete Fourier transform: signal from t = 20-140 µs

(a)

(b)

Figure 11. Graphs of signal amplitude and filtered signal amplitude for a 45º steering angle: (a) signal at x = 100 mm; and (b) band-pass filter = 0.7825-0.9825 MHz: signal from t = 20-140 µs

peaks, as the 30º steering angle's maximum peak is close to taking up the y-axes of both the simulated and experimental graphs, compared to the 15º steering angle's maximum simulated peak being approximately a third of the y-axis, and the maximum experimental peak being approximately a tenth of its y-axis.

There is also a similarity in the peaks following the direct shear wave. Figure 13 shows a comparison of the experimental results with the simulated results for the 60º steering angle at the backwall x-position of 115 mm. The experimental results show a smaller peak and then a larger peak following the direct shear wave peak. The smaller peak was determined to be the shear wave reflected from the sidewall and the larger peak the Rayleigh waves that travelled across the surface, sidewall and backwall to the x-position. These waves made it through the band-pass filter due to them being of the same frequency as the pulse. Normalising both the amplitude and displacement could be used to calculate a correlation coefficient of 0.7870 between the two signals, indicating a strong correlation.

5. Steering capabilities

This study has focused on the four steering angles of 15º, 30º, 45º and 60º, by running simulations of the experimental set-up and then validating the results in the laboratory. As a result of simulation validation, further simulations were undertaken at steering angles that were left out of the study, so that a better picture of the transmit-EMAT's steering capability could be perceived. The total time it took to run the 15º simulation was 52 h and thus it was decided not to run simulations for any steering angle below this due to time constraints and equipment limitations. Simulations of steering angles between 15-90º at every 5º interval were also run with the same set-up as the initial models, with differing time-steps and mesh densities to account for the different frequencies (and thus different CFL values) and the same results across the aluminium block's backwall were also recorded.

For every simulated steering angle, the backwall x-position with the largest direct shear wave displacement magnitude was used to calculate the angle of that shear wave. From this x-position, the value of the displacement magnitude was also recorded. To examine how changing the steering angle affects the transmission of Rayleigh waves, values of the displacement magnitude from the surface 100 mm to the right of the transmit-EMAT were recorded. The results of these simulations are summarised in Figure 14.

As the steering angle increases from 15-25º, the shear wave angle directly correlates with the steering angle. As the steering angle increases from 30-40º, the shear wave angle seems to plateau, until it increases to 45º and the shear wave angle recorrelates with the steering angle. When the steering angle reaches 50º, the shear wave angle starts to plateau and reaches its maximum at 60º.

As the steering angle increases: the shear wave displacement gradually increases (15-25º); reaches a peak (30º); gradually decreases (35-40º); and reaches a plateau (45º). The Rayleigh wave was only measurable for steering angles between 30-90º, as from 15-25º it was too small to be reliably recorded. From 30º, the Rayleigh wave displacement gradually increases until approximately 60º, when it starts to reach a peak at 90º.

From Figure 14, it can be seen that the Rayleigh wave displacement starts to overtake the shear wave displacement
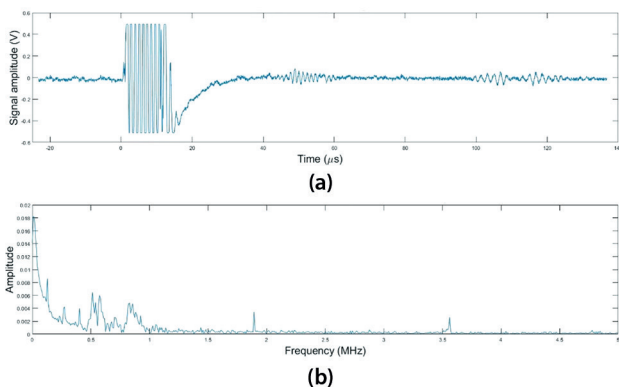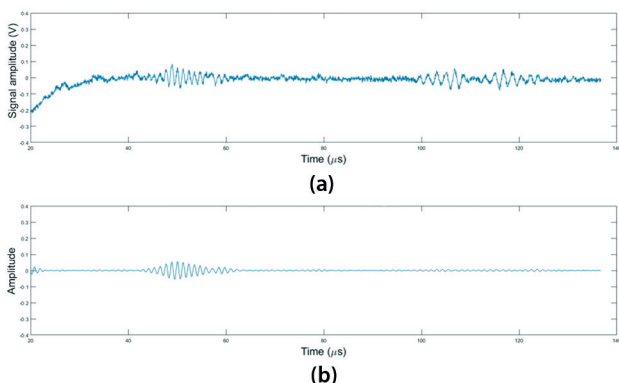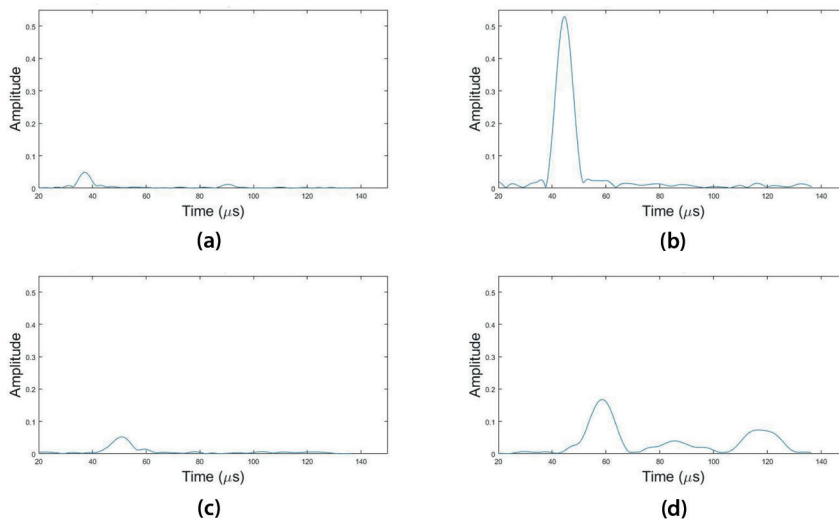
Figure 12. Graphs of filtered signal amplitude envelope *versus* time for each steering angle: (a) 15º steering angle: amplitude at *x* = 30 mm; (b) 30º steering angle: amplitude at *x* = 70 mm; (c) 45º steering angle: amplitude at *x* = 100 mm; (d) 60º steering angle: amplitude at *x* = 115 mm
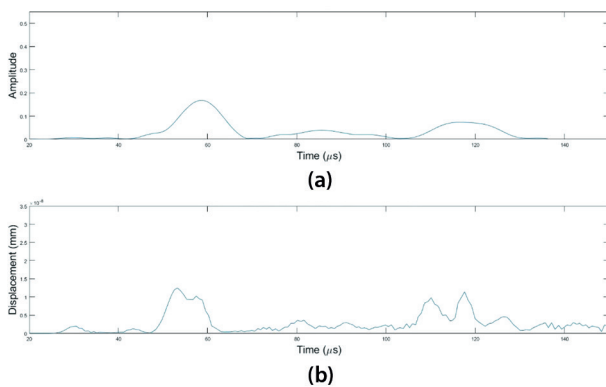

Figure 13. Experimental and simulated results for a 60º steering angle: (a) amplitude at *x* = 115 mm; and (b) displacement at *x* = 115 mm

between a steering angle of 45-50º, approximately the same as the steering limit. The maximum shear wave displacement is produced at a steering angle of approximately 30º, approximately the same steering angle that causes inconsistencies in the correlation between the steering angle and the shear wave angle.
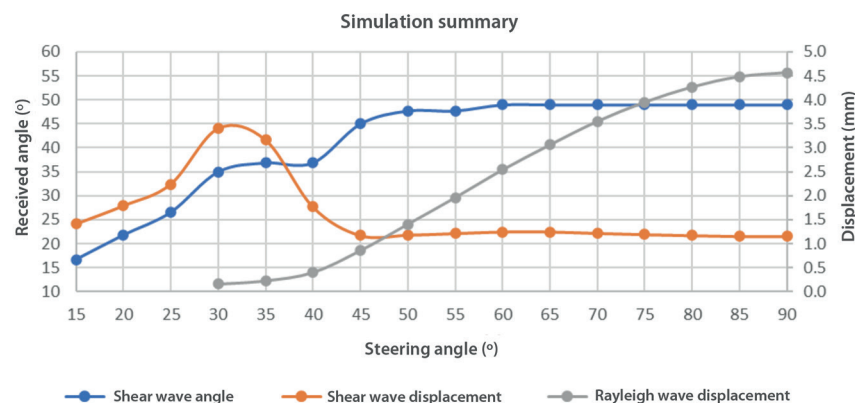

Figure 14. Effects of steering angle on shear wave angle, shear wave displacement and Rayleigh wave displacement

6. Conclusion

Over the course of this study, the objective was to simulate and experimentally validate the bulk wave steering capability of an MLC EMAT on aluminium for different steering angles. The COMSOL simulations seemed to reliably correlate with the experimental validations. The differences in the simulated and experimental results were determined to be due to the differences in their set-ups: simulations having a time delay in their wave transmissions explaining their earlier arrival time and experiments requiring a changing capacitance value in the receive-EMAT explaining their weaker SNR.

Simulations across a wider range of steering angles produced results that gave interesting conclusions. As the steering angle increases from 15-25º, the shear wave angle and displacement gradually increases. As the steering angle increases from 30-40º, the shear wave angle starts to plateau and the shear wave displacement peaks before gradually decreasing. As the steering angle increases from 45-90º, the shear wave angle plateaus at approximately 50º, the shear wave displacement plateaus at approximately 1.2×10^{-8} mm and the Rayleigh wave displacement overtakes the shear wave displacement and continues to increase to the maximum steering angle of 90º. Based on this, it can be concluded that the steering limit of this MLC transmit-EMAT is approximately 50º.

Further investigations would involve changing the coil spacing to observe how this affects the steering limit and test on a semi-circular specimen to better measure the angles and displacements of both the shear and compression waves with a changing steering angle. For future industrial work, the MLC EMAT could be adapted for deployment on an automated scanning system, along with the use of coded excitation signals to improve the SNR[24] for internal flaw detection and weld joint inspection.

Acknowledgements

References

1. M Hirao and H Ogi, EMATs for Science and Industry: Non-Contacting Ultrasonic Measurements, Kluwer Academic Publishers, Boston, Massachusetts, USA, 2003.
2. R Ribichini, F Cegla, P B Nagy and P Cawley, 'Experimental and numerical evaluation of electromagnetic acoustic transducer performance on steel materials', NDT&E International, Vol 45, No 1, pp 32-38, August 2011.

3. O Rees-Lloyd, P Charlton, S Mosey and R Lewis, 'Effects of relative motion on a Rayleigh wave electromagnetic acoustic transducer operating on aluminium', Insight: Non-Destructive Testing and Condition Monitoring, Vol 61, No 2, pp 83-89, February 2019.

4. ASTM E1816-12, 'Standard practice for ultrasonic testing using electromagnetic acoustic transducer (EMAT) techniques', August 2018.

5. X Jian, S Dixon, K Grattan and R S Edwards, 'A model for pulsed Rayleigh wave and optimal EMAT design', Sensors and Actuators A: Physical, Vol 128, No 2, pp 296-304, April 2006.

6. L Kang, S Dixon, K Wang and J Dai, 'Enhancement of signal amplitude of surface wave EMATs based on 3D simulation analysis and orthogonal test method', NDT&E International, Vol 59, No 1, pp 11-17, October 2013.

7. J K Hu, Q L Zhang and D A Hutchins, 'Directional characteristics of electromagnetic acoustic transducers', Ultrasonics, Vol 26, pp 5-13, January 1988.

8. G A Alers and L R Bums, 'EMAT designs for special applications', Materials Evaluation, Vol 45, No 10, pp 1184-1194, October 1987.

9. R B Thompson, 'Physical principles of measurements with EMAT transducers', Physical Acoustics, Vol 19, pp 157-200, 1990.

10. K Sawaragi *et al*, 'Improvement of SH-wave EMAT phased array inspection by new eight-segment probes', Nuclear Engineering and Design, Vol 198, pp 153-163, September 1999.

11. H Sun *et al*, 'Oblique point-focusing shear-horizontal guided wave electromagnetic acoustic transducer with variable PPM spacing', IEEE Transactions on Ultrasonics, Ferroelectrics, and Frequency Control, Vol 67, No 8, pp 1691-1700, August 2020.

12. S Hill and S Dixon, 'Frequency dependent directivity of periodic permanent magnet electromagnetic acoustic transducers', NDT&E International, Vol 62, pp 137-143, January 2014.

13. H Gao and B Lopez, 'Development of single-channel and phased array electromagnetic acoustic transducers for austenitic weld testing', Materials Evaluation, Vol 68, No 7, pp 821-827, July 2010.

14. S Hill and S Dixon, 'Localisation of defects with time and frequency measurements using pulsed arrays', NDT&E International, Vol 67, pp 24-30, June 2014.

15. B W Drinkwater and P D Wilcox, 'Ultrasonic arrays for non-destructive evaluation: a review', NDT&E International, Vol 39, No 7, pp 525-541, October 2006.

16. J A Jensen, S I Nikolov, K L Gammelmark and M H Pedersen, 'Synthetic aperture ultrasound imaging', Ultrasonics, Vol 44, pp e5-e15, August 2006.

17. H Ogi and M Hirao, 'Line-focusing of ultrasonic SV wave by electromagnetic acoustic transducer', The Journal of the Acoustical Society of America, Vol 103, No 5, pp 2411-2415, May 1998.

18. H Ogi, M Hirao and T Ohtani, 'Line-focusing electromagnetic acoustic transducers for the detection of slit defects', IEEE Transactions on Ultrasonics, Ferroelectrics, and Frequency Control, Vol 46, No 2, pp 341-346, March 1999.

19. H Sun, S Huang, S Wang and W Zhao, 'Meanderline coil arrangement of ultrasonic wave line-focusing electromagnetic acoustic transducers', 2020 IEEE International Instrumentation and Measurement Technology Conference (I2MTC), May 2020.

20. T J Moran and R M Panos, 'Electromagnetic generation of electronically steered ultrasonic bulk waves', Journal of Applied Physics, Vol 47, No 5, pp 2225-2227, May 1976.

21. Y Wu *et al*, 'Effect of coil configuration on conversion efficiency of EMAT on 7050 aluminium alloy', Energies, Vol 10, No 10, September 2017.

22. D Ratnam, A Kuamr and P C R Bhagi, 'Time-domain finite element modelling of pulsed meander coil electromagnetic acoustic transducer', Electromagnetic Non-Destructive Evaluation (XXI), Vol 43, pp 246-254, May 2018.

23. R Courant, K O Friedrichs and H Lewy, 'On the partial difference equations of mathematical physics', IBM Journal of Research and Development, Vol 11, No 2, pp 215-234, March 1967.

24. J Isla and F B Cegla, 'Coded excitation for pulse-echo systems', IEEE Transactions on Ultrasonics, Ferroelectrics, and Frequency Control, Vol 64, No 4, pp 736-748, April 2017.